



# Ultra-high throughput manufacturing method for composite solid-state electrolytes

**Journal Article****Author(s):**

Baade, Paul ; Wood, Vanessa 

**Publication date:**

2021-02-19

**Permanent link:**

<https://doi.org/10.3929/ethz-b-000465618>

**Rights / license:**

[Creative Commons Attribution-NonCommercial-NoDerivatives 4.0 International](#)

**Originally published in:**

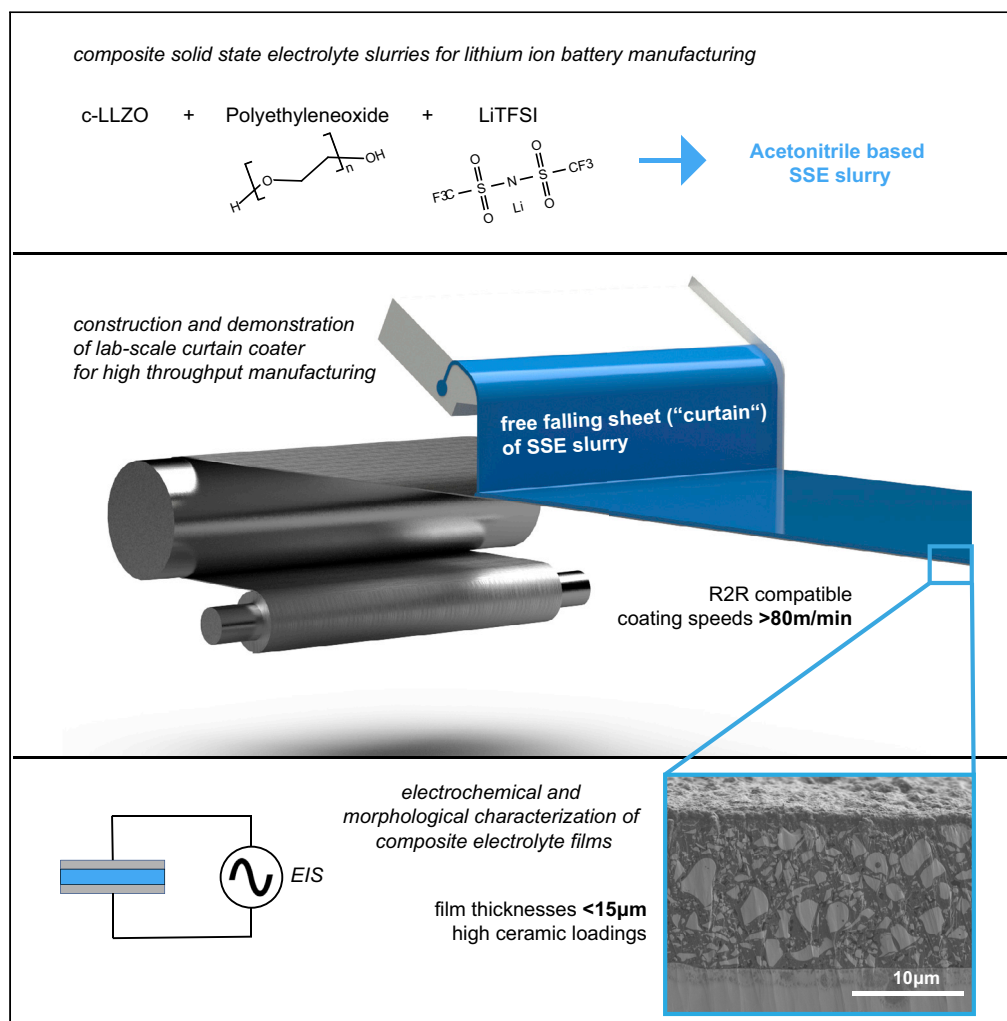
iScience 24(2), <https://doi.org/10.1016/j.isci.2021.102055>

**Funding acknowledgement:**

680070 - Development of Quantitative Metrologies to Guide Lithium Ion Battery Manufacturing (EC)

## Article

## Ultra-high throughput manufacturing method for composite solid-state electrolytes

Paul Baade,  
Vanessa Wood

vwood@ethz.ch

**HIGHLIGHTS**

Demonstration of curtain coating to manufacture composite solid state electrolytes

Compatibility with existing battery manufacturing infrastructure

Realization of high coating speeds (>80m/min) for thin films (<15µm)

Untapped potential for engineering solutions for solid state batteries

Baade & Wood, iScience 24, 102055  
February 19, 2021 © 2021 The Authors.  
<https://doi.org/10.1016/j.isci.2021.102055>

## Article

## Ultra-high throughput manufacturing method for composite solid-state electrolytes

Paul Baade<sup>1</sup> and Vanessa Wood<sup>1,2,\*</sup>

## SUMMARY

**The transition from liquid organic electrolytes to solid-state electrolytes promises safer and more energy-dense lithium ion batteries. Although this technology has been demonstrated, the question of how to manufacture solid-state batteries at the cost and scales needed to be competitive remains. Here we propose and demonstrate curtain coating as a method for manufacturing composite solid-state electrolytes in roll-to-roll processes at web-speeds of over 80 m/min. The method is compatible with existing lithium-ion battery electrode manufacturing lines and is able to produce uniform electrolyte films with thicknesses below 15 micrometers.**

## INTRODUCTION

Currently the majority of lithium ion batteries produced rely on liquid electrolytes, where a lithium salt is dissolved in one or more organic solvents combined with additives to enhance performance and safety (Blomgren, 2017; Kwade et al., 2018). However, all solid-state batteries, where the liquid electrolyte is replaced with a solid is expected to become a dominant technology in the coming years. Over the last decade, the room temperature ionic conductivities have increased up to  $10^{-2}$  S/cm for inorganic electrolytes, and solid polymer electrolytes typically exhibit conductivities around  $10^{-6}$  S/cm at room temperature (Murata et al., 2000; Fergus, 2010; Fan et al., 2018; Gao et al., 2018), making fast charge and discharge of all solid-state cells a possibility. Many solid-state electrolytes offer large electrochemical windows, opening the path for high-voltage cathodes and lithium metal anodes and thereby increasing the specific energy density (Janek and Zeier, 2016; Manthiram et al., 2017; Zhang et al., 2018; Liu et al., 2019). Solid-state electrolytes allow exploration of new cell designs, such as thin-format (Sastre et al., 2019), flexible cells (Chen et al., 2019), or bipolar stacking (Kim et al., 2018). Although the safety of solid-state technology still requires further investigation (Wang et al., 2019), the non-flammability of the electrolyte makes them safer than the liquid electrolyte alternative.

However, solid-state batteries place new requirements on manufacturing (Kerman et al., 2017; Schnell et al., 2018). Although 100- $\mu$ m thicknesses are standard for porous electrodes, electrode and electrolyte film thicknesses of less than 30  $\mu$ m are desirable in solid-state technology to keep diffusion lengths short and facilitate capacity extraction at elevated currents (Kwade et al., 2018; Schnell et al., 2018). Furthermore, these thin films must be uniform and crack-free to ensure an even current density distribution and prevent lithium dendrites, which can lead to safety concerns such as short circuiting. Finally, the interfaces between the electrolyte and the active material in solid-state technology are solid-on-solid, instead of liquid-on-solid. To ensure a sufficient cycle life, solid-state technology thus requires additional interface engineering for adhesion and mechanical compliance directly at the electrode manufacturing step.

Because competitive advantage in battery manufacturing stems largely from economies of scale, to tap into markets such as electric vehicles, solid-state batteries have to be manufactured at a high throughput. Today, porous electrodes are manufactured at web speeds of up to 50m/min (Kwade et al., 2018; Hawley and Li, 2019) by double-sided slot coating and subsequent drying. Taking a foil width of 1.5m into account, this roughly translates to a throughput of 150 m<sup>2</sup>/min for the roll-to-roll coating lines (Nelson et al., 2012).

Figure 1 summarizes the parameter space of existing vapor phase and wet-coating deposition techniques in terms of throughput (given as a coverage speed in m<sup>2</sup>/min) and achievable film thicknesses (Schnell et al., 2019). This plot highlights that manufacturing the thin films needed for solid-state electrolyte and electrode layers is difficult at high throughput.

<sup>1</sup>Department of Information Technology and Electrical Engineering, Materials and Device Engineering Group, ETH Zurich, 8092 Zürich, Switzerland

<sup>2</sup>Lead contact

\*Correspondence: wood@ethz.ch

<https://doi.org/10.1016/j.isci.2021.102055>



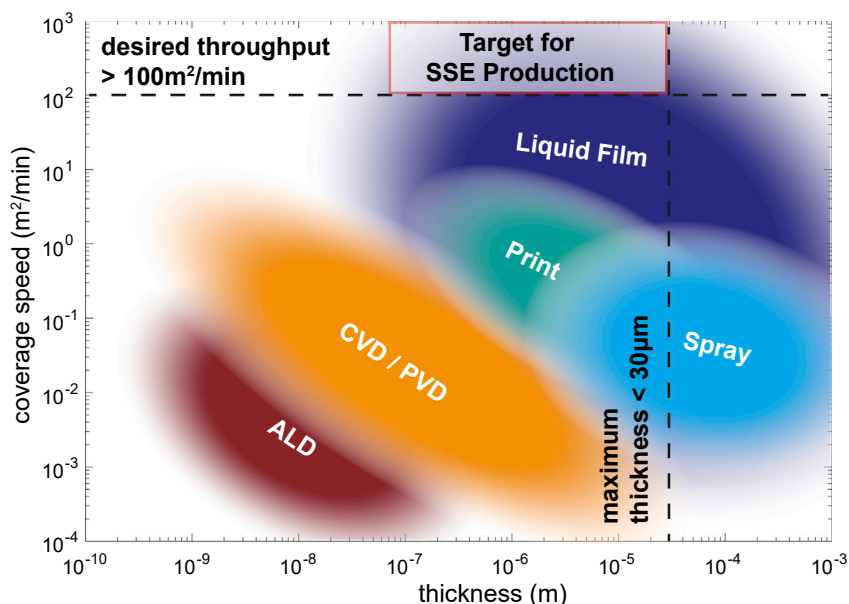


**Figure 1. Approaches to solid-state battery manufacturing**

Solid-state electrolytes and electrodes (SSEs) must be thin ( $<30\ \mu\text{m}$ ) and produced at high throughput ( $>100\ \text{m}^2/\text{min}$ ). Typical thicknesses and coverage speeds for different, mature thin film manufacturing technologies are given.

Although thin films can be readily achieved through vapor phase deposition approaches, and vapor phase deposition is standard for solid-state batteries in the microelectronics industry (Liang et al., 2019), technologies are still a long way off from providing sufficient throughput in terms of GWh/year production. Vapor-based technologies can be used in a roll-to-roll configuration, and higher coverage could be achieved by installation of parallel lines; however, the investment for vapor phase technologies is typically higher compared with wet coating alternatives. At the same time, although printing and spray technologies are already near the target throughput at desirable thicknesses, implementation of a wet-coating, roll-to-roll process would lower the adoption barrier for solid-state technology, as existing equipment can be retrofitted and know-how can be leveraged.

Here we explore the potential of curtain coating. Curtain coating is a wet-coating, roll-to-roll compatible process that offers ultra-high throughput production of thin layers and has not yet been explored as an approach to solid-state electrolyte manufacturing. Curtain coating has been a workhorse for the paper, packaging, and photographic film industry and has recently been explored for polymer electrolytes, electronics, and solar cells and ceramic coating of separators (Licari, 2003; Döll, 2010; Søndergaard et al., 2012; Arnold et al., 2015; Chen et al., 2015a, 2015b). The principles of curtain coating are illustrated in Figures 2A and 2B. A slurry is pumped from a reservoir to a coating die elevated above the substrate. As the slurry exits the die through a slit, a liquid sheet or “curtain” forms (Miyamoto and Katagiri, 1997). For stable operation, the inertial force of the curtain must be greater than the surface tension (Weber Number,  $We > 2$ ) (Brown, 1961). Unlike self-metered techniques (e.g., tape, gravure printing), which depend strongly on liquid and environmental properties, curtain coating is a pre-metered technique meaning that the resulting wet thickness,  $h_{wet}$ , can easily be tuned by changing the flow rate,  $Q$ , or web speed,  $v_{web}$ , according to:  $h_{wet} = Q/v_{web}$ . Furthermore, in contrast to other pre-metered deposition technologies such as slot die coating, curtain coating benefits from an effect called hydrodynamic assist (Blake et al., 1994; Blake et al., 2015; Liu et al., 2016). The free-falling curtain creates a pressure field at the point of impingement of the curtain on the substrate. The inertia of the curtain delays the onset of air entrainment. This enables coating speeds faster than 2000 m/min and dry film thicknesses less than  $1\ \mu\text{m}$ , exceeding state of the art in slot die coating and beating other liquid film technologies (Miyamoto and Katagiri, 1997; Döll, 2010).

We take the first steps toward demonstrating curtain coating as an approach to high-throughput manufacturing of solid-state lithium-ion batteries. Using a lab-scale curtain coater and conveyor line, we produce uniform thin films of composite solid-state electrolytes at a rate of  $\sim 80\ \text{m}/\text{min}$  with thicknesses below  $15\ \mu\text{m}$  and ionic conductivity in line with literature values.

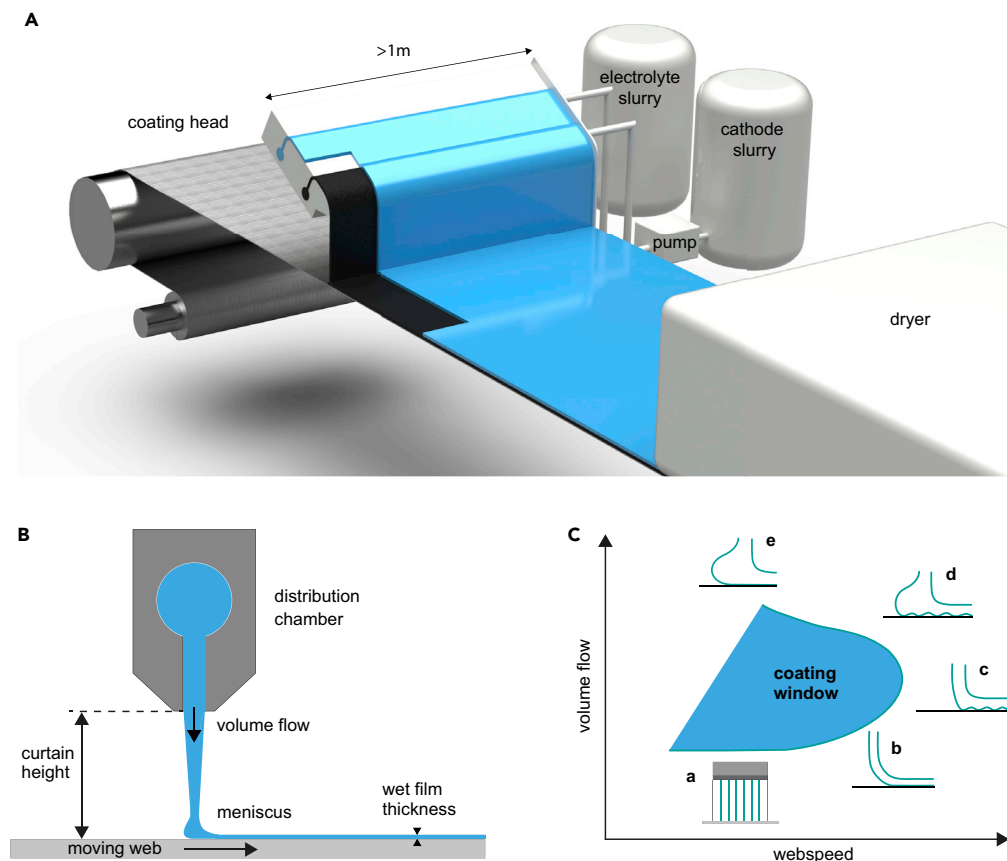


**Figure 2. Curtain coating**

(A) Industrial implementation of a multilayer curtain for a roll-to-roll fabrication. The cathode slurry (black) and the electrolyte slurry (blue) form a single curtain and are deposited simultaneously and subsequently dried.

(B) A cross-sectional schematic view of a curtain coating setup with the relevant descriptors marked.

(C–E) (C) For a given slurry composition, there will be a range of web speeds and volume flows that permit a stable curtain and uniform coating (i.e., the coating window). If the volume flow is too low, the curtain can disintegrate (case a). If the web is too fast, the curtain can get pulled (case b) or air entrainment causes defects (cases c and d). If the volume flow is too high, a heel forms (d and e).

## CURTAIN COATING

To validate curtain coating for ultra-high-speed throughput manufacturing of composite solid-state electrolytes, we design and construct a curtain coating setup that enables realistic operation speed and slurries, while being suitable for lab-scale operation with minimal footprint and material usage (Figures 3A, S1, and S2). The wet film thickness is controlled by regulating the volume flow (up to 2500 mL/min) and the substrate speed (up to 3.5 m/s).

For successful curtain coating, the rheological properties of the slurry (e.g., solid content, viscosity) and its deposition parameters (e.g., volume flow and web speed) must be optimized (Figure 2C). When the volume flow is too low, a stable curtain cannot be established (Case a). The sheet disintegrates and runs down in individual streaks (Video S3). At relatively slow speeds and low flow rates, the curtain is bent and leads to a pulled film (Case b). The wetting line shifts downstream and the coating processes cannot benefit properly from the hydrodynamic assist. In particular, slight disturbances can cause the curtain to break up, because this point of operation is very close to instability. Air entrainment limits the maximum coating speed (Case c). It sometimes occurs in combination with heel formation (Case d) and needs to be avoided to achieve a smooth and uniform film. High volume flows in general cause a heel to form behind the point of impingement where slurry recirculates (Case e), which can trap bubbles, agglomerate or gel. With the coating window identified, it is possible to calculate the volume flow and the web speed needed to achieve a specific wet film thickness.

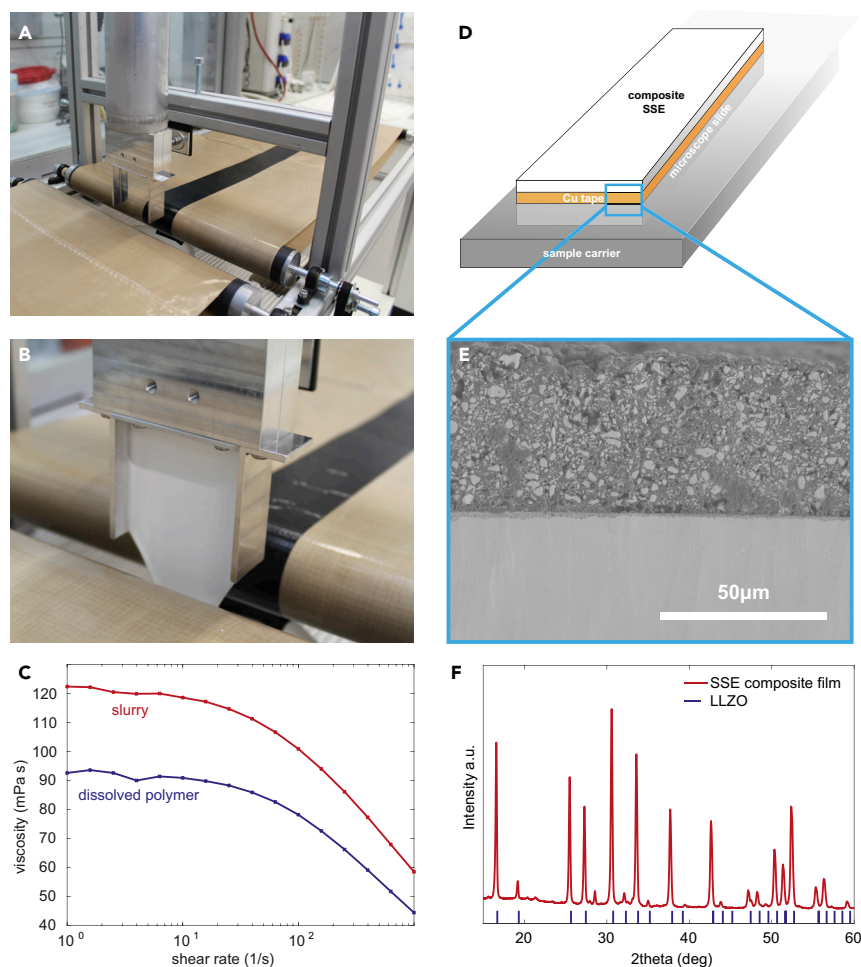


**Figure 3. Pilot curtain coating of composite solid-state electrolyte**

(A) Photograph of the pilot curtain coater

(B) Photograph of stable curtain (4.5 cm curtain height) of LLZO, PEO, and LiTFSI in acetonitrile.

(C) Rheological properties of slurry and that of PEO (without LLZO) in acetonitrile.

(D) To minimize material waste as coating parameters (e.g., volume flow and web speed) are adjusted, segments of the copper foil are affixed to carriers.

(E) A scanning electron microscopy (SEM) cross-section of an as-deposited composite electrolyte film (scale bar is 50 μm).

(F) X-ray diffraction (XRD) pattern of the as-deposited composite electrolyte film with an LLZO standard is provided.

As a model system, we choose to work with a polymer-ceramic composite electrolyte that has been extensively studied in literature (Fu et al., 2016; Zheng et al., 2016; Chen et al., 2018; Liu et al., 2018; Yao et al., 2019): Al-doped lithium lanthanum zirconate (LLZO) and polyethylene oxide (PEO) (in a 4.45:1 mass ratio) with lithium bis(trifluoromethanesulfonyl)imide (LiTFSI) salt (molar ratio of EO:Li at 10.4:1). To form the slurry, the LLZO, PEO, and LiTFSI are mixed in anhydrous acetonitrile (17.5% solid content).

A close-up image (Figure 3B) shows a stable curtain. Rheological measurements show that the slurry exhibits shear thinning behavior and a viscosity of 60 mPa s at a shear rate of 1000 1/s (Figure 3C). The rheological properties of the slurry mimic the trends of the polymer phase, highlighting the possibility to tune it based on the molecular weight of the polymers or by using combinations of different polymers. The slurry did not show any phase separation; however, during coating, the slurry is agitated in the reservoir to avoid agglomerations and gradual sedimentation.

During the coating trials, web speeds of 41.7 m/min and 83.4 m/min are used (Videos S1 and S2). With a volume flow of 1327 mL/min, this should lead to dried film thicknesses of 15.2 μm and 30.5 μm

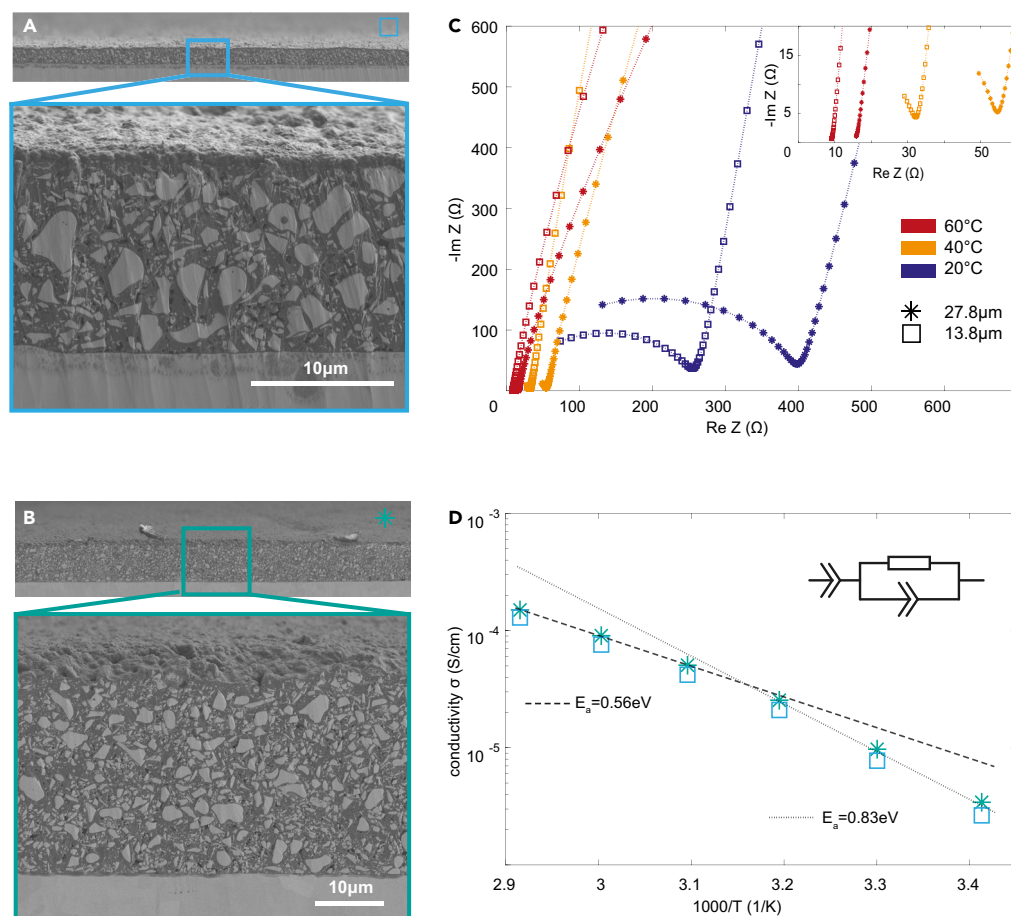


**Figure 4. Electrochemical performance of curtain-coated solid-state electrolyte thin film**

(A and B) Scanning electron microscopy (SEM) images of (A) thin and (B) thick solid-state electrolyte film following calendaring under heat (scale bars are 10 μm).

(C) Electrochemical impedance spectroscopy of thin (\* symbol) and thick (square symbol) films at 20, 40, and 60 (C).

(D) Conductivities for both the thin film (\* symbol) and thick film (square symbol) match.

(Table S1), and the measured results of 13.8 μm and 27.8 μm are in good agreement. No air entrainment is observed and the films show no streaking defects, suggesting that these web speeds are indeed within the coating window.

Following deposition of the slurry on the copper foil, the solvent is evaporated at 60°C under vacuum. Cross-sectional scanning electron microscopy (SEM) image of an as-deposited film highlights that the coating process results in uniform films (Figure 3D). The XRD pattern (Figure 3F) of the coated film shows that the LLZO is present in the high conductivity cubic phase and that the PEO is amorphous (broad peak in the background) due to the high concentration of the Li salt (Figure S3).

Finally, hot pressing of the completed films allows the polymer to redistribute and fill voids and promote adhesion with the metallic current collector and between the polymer and ceramic, which enhances the mechanical properties and electrochemical performance (Chen et al., 2018).

## RESULTS

SEM cross-sections of the solid-state electrolyte films shown in Figures 4A and 4B reveal a uniform distribution of ceramic particles in a polymer matrix and minimal thickness variations for both coating speeds. The scale space analysis (Figure S4) reveals a uniform morphology on a length scale of approximately 13.5 micrometers. A top view of the films is provided in Figure S5. To demonstrate that the lithium ion transport

properties of these thin films fabricated with curtain coating are similar to those reported in thicker LLZO/PEO ceramic composites, we perform electrochemical impedance spectroscopy (EIS) (Figures 4C and S6), and fit the EIS data with an equivalent circuit model consisting of a bulk resistance  $R_{\text{bulk}}$  and constant phase element  $\text{CPE}_{\text{bulk}}$  in parallel, and an additional  $\text{CPE}_{\text{blocking}}$  in series to represent the blocking electrodes (Table S2). As expected for thermally activated lithium transport, as temperature increases, the conductivity increases from  $3 \times 10^{-6}$  S/cm at 20°C to  $1.6 \times 10^{-4}$  S/cm at 70°C. The 13.8- $\mu\text{m}$  and 27.8- $\mu\text{m}$  thick films exhibit the same conductivity, indicating the uniformity of the manufacturing process at different web speeds. Activation energies of the lithium hopping are found to be 0.83eV (below 40°C) and 0.56eV (above 40°C) (Figure 4D). These values suggest that lithium ion conduction in the film is dominated by the polymer matrix.

## DISCUSSION

This proof-of-concept realization of curtain coating of composite electrolytes shows that curtain coating is a technique that merits further exploration for solid-state battery manufacturing. We demonstrated  $\sim 80$  m/min production of uniform thin films of LLZO-PEO electrolyte with thicknesses below 15  $\mu\text{m}$  and electrochemical performance on par with that expected for the given material system. We used a high ceramic content (4.45:1 LLZO-PEO by mass) and a slurry with high solid content for curtain coating (17.5%), resulting in a thin film with 37.2% ceramic by volume (Figure S4) to show the potential for curtain coating of solid-state electrodes with ceramic active particles.

Curtain coating offers a clear path to address the current bottlenecks associated with solid-state battery manufacturing (Wang et al., 2020): it could enable high-throughput manufacturing compatible with existing infrastructure decreasing the barriers to market adoption and it offers new solutions for interface engineering. The implementation of curtain coating in other industries has proven that it can be carried out as a roll-to-roll process in conjunction with drying units as is currently used in the lithium battery industry for electrode fabrication. Furthermore, by using a series of reservoirs and slots within the coating head, multi-layer curtain coating is possible (Döll, 2010; Søndergaard et al., 2012), which, for solid-state technology, for example, could enable simultaneous deposition of a cathode and solid-state electrolyte layer for subsequent assembly with a lithium metal anode and current collector.

In term of improved interfaces and mechanical stability, curtain coating offers attractive opportunities. First, curtain coating works inherently well with a polymer electrolyte. The polymer helps obtain a large and stable coating window so that web speeds and thus film thicknesses can be varied over a wide range. At the same time, use of a polymer is an accepted approach to solving adhesion and mechanical stability issues in solid-state battery technology (Yao et al., 2019; Li et al., 2020). The application of heat during calendaring results in dense films with excellent adhesion between the ceramic and polymer as the current collector. The possibility to incorporate lower molecular weight polymers or even polymers that are thermally activated by the hot-pressing process could be used to further enhance interface stability, contact with solid particles, and electrochemical performance. Second, the possibility of multilayer coating means that layers can be formed in parallel, enabling gap-free interfaces.

## Limitations of the study

In this study, the selection of the LLZO-PEO composite was useful for a proof-of-concept; however, it does not represent a thin film optimized for electrochemical performance. Significant work has already been carried out to optimize electrochemical performance of the electrolyte films, and this knowledge can be leveraged in the development of slurries for curtain coating. The work of Li et al. provides a good overview of composite systems that range from 1wt% to 70wt% content of inorganic lithium-ion conducting materials (Li et al., 2020). The optimal choice depends strongly on size and shape of the fillers and the resulting morphology. Here, the ceramic content was set relatively high at about 80wt% to highlight that curtain coating can be used for solid-state layers with ceramic active particles. More generally, our choice of a composite polymer-ceramic electrolyte was used to highlight the ease in obtaining a wide coating window with a polymer and how a polymer component facilitates the creation of dense films via thermal annealing.

In principle, curtain coating is material independent and would thus be compatible with other solid-state electrolytes (e.g., garnet-, perovskite-, sulfide-, NASICON-type, inert oxides) as well as solid-state electrolyte-active material mixtures to achieve all solid-state batteries (Famprakis et al., 2019; Yao et al., 2019). However, for any material system, a suitable slurry formulation must be developed, which involves tuning



the solid content (morphology and amount of solid phase (Strauss et al., 2018; Froboese et al., 2019)) and selection of the solvent. Some material systems need special processing conditions (e.g. moisture free) or additional post-processing steps (e.g., high temperature annealing), which could be a time-limiting step. In this case, careful consideration of how to optimize the slurry for rapid post-processing and how to adapt the manufacturing line is needed. For example, the length of the manufacturing line could be extended (in current lithium-ion battery manufacturing, long lines with more drying units are used to enable faster web speeds while ensuring sufficient dwell time) or roll-to-roll compatible systems used in the solar cell industry such as rapid thermal annealing could be leveraged.

Curtain coating offers the potential of high-throughput manufacturing. With commercial manufacturing equipment, web speeds can be increased beyond the 80 m/min reported here, but range of web speeds is ultimately dependent on slurry rheology. High viscosities and high solid contents slurries that are common for electrodes are not compatible with the extremely high curtain coating web speeds of >2000m/min used in other industries. Although curtain coating is not amenable to double-sided coating of electrodes (which is often used to save time in battery manufacturing plants today), curtain coating offers faster web speeds as well as the opportunity for multilayer coating, with the possibility of double-sided coating performed sequentially.

In summary, curtain coating should be explored further as a manufacturing technique for solid-state batteries to alleviate some of the key bottlenecks to their adoption and widespread commercialization.

### Resource availability

#### Lead contact

Further information and requests for resources and reagents should be directed to and will be fulfilled by the Lead Contact, Vanessa Wood ([vwood@ethz.ch](mailto:vwood@ethz.ch)).

#### Materials availability

This study did not generate new unique reagents.

#### Data and code availability

The published article includes all datasets generated or analyzed during this study.

## METHODS

All methods can be found in the accompanying [Transparent methods supplemental file](#).

## SUPPLEMENTAL INFORMATION

Supplemental information can be found online at <https://doi.org/10.1016/j.isci.2021.102055>.

## ACKNOWLEDGMENTS

P.B. and V.W. acknowledge support from a European Research Council Starting Grant (n. 680070), an ETH Research Grant, and a grant from the Strategic Focus Program - Advanced Manufacturing.

## AUTHOR CONTRIBUTIONS

Conceptualization, P.B. and V.W.; Methodology, P.B. and V.W.; Investigation, P.B.; Writing—Original Draft, P.B.; Writing—Review & Editing, P.B. and V.W.; Funding Acquisition, V.W.; Resources, P.B.; Supervision, V.W.

## DECLARATION OF INTERESTS

The authors declare no competing interests.

Received: October 13, 2020

Revised: November 3, 2020

Accepted: January 7, 2021

Published: February 19, 2021

## REFERENCES

- Nelson, P.A., Gallagher, K.G., Bloom, I., and Dees, D.W. (2012). Modeling the Performance and Cost of Lithium-Ion Batteries for Electric-Drive Vehicles (Argonne National Laboratory).
- Arnold, J., Fasolo, J., and Voelker, G.E. (2015). Polymer-bound Ceramic Particle Battery Separator Coating, WO2015057815A1. <https://worldwide.espacenet.com/patent/search/family/052826449/publication/WO2015057815A1?q=pn%3DWO2015057815A1>.
- Chen, X., Huang, H., Pan, L., Liu, T., and Niederberger, M. (2019). Fully integrated design of a stretchable solid-state lithium-ion full battery. *Adv. Mater.* 31, 1–10.
- Chen, L., Li, Y., Li, S., Fan, L., Nan, C., and Goodenough, J.B. (2018). 'PEO/garnet composite electrolytes for solid-state lithium batteries: from "ceramic-in-polymer" to "polymer-in-ceramic"'. *Nano Energy* 46, 176–184.
- Chen, Y., Cheng, W., Guan, C., Jiang, H., Li, X., Zhang, S., and Zhao, J. (2015a). Composite Porous Separator and Electrochemical Device, US2015280197A1. <https://worldwide.espacenet.com/patent/search/family/050995506/publication/US2015280197A1?q=pn%3DUS2015280197A1>.
- Chen, L., Ma, C., Wei, W., Zhang, J., et al. (2015b). All-solid-state polymer electrolyte for surface chemical grafting inorganic particles and preparation method of all-solid-state polymer electrolyte (Espacenet), CN104600358A. <https://worldwide.espacenet.com/patent/search/family/053125988/publication/CN104600358A?q=pn%3DCN104600358A>.
- Blake, T.D., Clarke, A., and Ruschak, K.J. (1994). Hydrodynamic assist of dynamic wetting. *Aiche J.* 40, 229–242.
- Blake, T.D., Fernandez-Toledano, J., Doyen, G., and De Coninck, J. (2015). Forced wetting and hydrodynamic assist. *Phys. Fluids* 27, 112101.
- Blomgren, G.E. (2017). The development and future of lithium ion batteries. *J. Electrochem. Soc.* 164, A5019–A5025.
- Brown, D.R. (1961). A study of the behaviour of a thin sheet of moving liquid. *J. Fluid Mech.* 10, 297–305.
- Döll, H. (2010). Curtain coating - when the curtain falls. *Wochenblatt für Papierfabrikation* 138, 483–488.
- Famprakis, T., Canepa, P., Dawson, J.A., Islam, M.S., and Masquelier, C. (2019). Fundamentals of inorganic solid-state electrolytes for batteries. *Nat. Mater.* 18, 1278–1291.
- Fan, L., Wei, S., Li, S., Li, Q., and Lu, Y. (2018). Recent progress of the solid-state electrolytes for high-energy metal-based batteries. *Adv. Energy Mater.* 8, 1–31.
- Fergus, J.W. (2010). Ceramic and polymeric solid electrolytes for lithium-ion batteries. *J. Power Sources* 195, 4554–4569.
- Froboese, L., Sichel, J.F.v. d., Loellhoeffel, T., Helmers, L., and Kwade, A. (2019). Effect of microstructure on the ionic conductivity of an all solid-state battery electrode. *J. Electrochem. Soc.* 166, A318–A328.
- Fu, K., Gong, Y., Dai, J., Gong, A., Han, X., Yao, Y., Wang, C., Wang, Y., Chen, Y., Yan, C., et al. (2016). Flexible, solid-state, ion-conducting membrane with 3D garnet nanofiber networks for lithium batteries. *Proc. Natl. Acad. Sci. U S A* 113, 7094–7099.
- Gao, Z., Sun, H., Fu, L., Ye, F., Zhang, Y., Luo, W., and Huang, Y. (2018). Promises, challenges, and recent progress of inorganic solid-state electrolytes for all-solid-state lithium batteries. *Adv. Mater.* 30, 1705702.
- Hawley, W.B., and Li, J. (2019). 'Electrode manufacturing for lithium-ion batteries—analysis of current and next generation processing'. *J. Energy Storage* 25, 100862.
- Janek, J., and Zeier, W.G. (2016). A solid future for battery development. *Nat. Energy* 1, 1–4.
- Kerman, K., Luntz, A., Viswanathan, V., Chiang, Y.-M., and Chen, Z. (2017). 'Review—practical challenges hindering the development of solid state Li ion batteries'. *J. Electrochem. Soc.* 164, A1731–A1744.
- Kim, S.H., Choi, K.H., Cho, S.J., Yoo, J., Lee, S.S., and Lee, S.Y. (2018). Flexible/shape-versatile, bipolar all-solid-state lithium-ion batteries prepared by multistage printing. *Energy Environ. Sci.* 11, 321–330.
- Kwade, A., Haselrieder, W., Leithoff, R., Modlinger, A., Dietrich, F., and Droeder, K. (2018). Current status and challenges for automotive battery production technologies. *Nat. Energy* 3, 290–300.
- Li, S., Zhang, S.Q., Shen, L., Liu, Q., Ma, J.B., Lv, W., He, Y.B., and Yang, Q.H. (2020). Progress and perspective of ceramic/polymer composite solid electrolytes for lithium batteries. *Adv. Sci.* 7, 1903088.
- Liang, X., Tan, F., Wei, F., and Du, J. (2019). Research progress of all solid-state thin film lithium Battery. *IOP Conf. Ser. Earth Environ. Sci.* 218, 012138.
- Licari, J.J. (2003). Manufacturing technology. In *Coating Materials for Electronic Applications*, J.J. Licari, ed. (Elsevier), pp. 201–277.
- Liu, C.-Y., Vandre, E., Carvalho, M.S., and Kumar, S. (2016). Dynamic wetting failure and hydrodynamic assist in curtain coating. *J. Fluid Mech.* 808, 290–315.
- Liu, X., Li, X., Li, H., and Wu, H.B. (2018). Recent progress of hybrid solid-state electrolytes for lithium batteries. *Chem. Eur. J.* 24, 18293–18306.
- Liu, J., Bao, Z., Cui, Y., Dufek, E.J., Goodenough, J.B., Khalifah, P., Li, Q., Liaw, B.Y., Liu, P., Manthiram, A., et al. (2019). Pathways for practical high-energy long-cycling lithium metal batteries. *Nat. Energy* 4, 180–186.
- Manthiram, A., Yu, X., and Wang, S. (2017). Lithium battery chemistries enabled by solid-state electrolytes. *Nat. Rev. Mater.* 2, 16103.
- Miyamoto, K., and Katagiri, Y. (1997). Curtain coating. In *Liquid Film Coating*, S.F. Kistler and P.M. Schweizer, eds. (Dordrecht: Springer), pp. 463–494.
- Murata, K., Izuchi, S., and Yoshihisa, Y. (2000). An overview of the research and development of solid polymer electrolyte batteries. *Electrochimica Acta* 45, 1501–1508.
- Schnell, J., Günther, T., Knoche, T., Vieider, C., Köhler, L., Just, A., Keller, M., Passerini, S., and Reinhart, G. (2018). 'All-solid-state lithium-ion and lithium metal batteries – paving the way to large-scale production'. *J. Power Sources* 382, 160–175.
- Sastre, J., Lin, T.Y., Filippin, A., Priebe, A., Avancini, E., Michler, J., Tiwari, A.N., Romanyuk, Y.E., and Buecheler, S. (2019). Aluminum-assisted densification of cosputtered lithium garnet electrolyte films for solid-state batteries. *ACS Appl. Energy Mater.* 2, 8511–8524.
- Schnell, J., Tietz, F., Singer, C., Hofer, A., Billot, N., and Reinhart, G. (2019). Prospects of production technologies and manufacturing costs of oxide-based all-solid-state lithium batteries. *Energy Environ. Sci.* 12, 1818–1833.
- Søndergaard, R., Hösel, M., Angmo, D., Larsen-Olsen, T.T., and Krebs, F.C. (2012). Roll-to-roll fabrication of polymer solar cells. *Mater. Today* 15, 36–49.
- Strauss, F., Bartsch, T., de Biasi, L., Kim, A.-Y., Janek, J., Hartmann, P., and Brezesinski, T. (2018). Impact of cathode material particle size on the capacity of bulk-type All-solid-state batteries. *ACS Energy Lett.* 3, 992–996.
- Wang, Q., Jiang, L., Yu, Y., and Sun, J. (2019). Progress of enhancing the safety of lithium ion battery from the electrolyte aspect. *Nano Energy* 55, 93–114.
- Wang, L., Li, J., Lu, G., Li, W., Tao, Q., Shi, C., Jin, H., Chen, G., and Wang, S. (2020). Fundamentals of electrolytes for solid-state batteries: challenges and perspectives. *Front. Mater.* 7, 1–5.
- Yao, P., Yu, H., Ding, Z., Liu, Y., Lu, J., Lavorgna, M., Wu, J., and Liu, X. (2019). Review on polymer-based composite electrolytes for lithium batteries. *Front. Chem.* 7, 1–17.
- Zhang, Z., Shao, Y., Lotsch, B., Hu, Y.-S., Li, H., Janek, J., Nazar, L.F., Nan, C.-W., Maier, J., Armand, M., and Chen, L. (2018). New horizons for inorganic solid state ion conductors. *Energy Environ. Sci.* 11, 1945–1976.
- Zheng, J., Tang, M., and Hu, Y.Y. (2016). Lithium ion pathway within Li7 La3 Zr2 O12 -polyethylene oxide composite electrolytes. *Angew. Chem. Int. Ed.* 55, 12538–12542.

**iScience, Volume 24**

**Supplemental Information**

**Ultra-high throughput manufacturing method  
for composite solid-state electrolytes**

**Paul Baade and Vanessa Wood**

## Transparent Methods

### Slurry preparation

$\text{Li}_{7-3x}\text{Al}_x\text{La}_3\text{Zr}_2\text{O}_{12}$  nano-powder was purchased from MSE supplies (Ampcera™ Al-doped LLZO). Polyethylene oxide powder (PEO, average  $M_v$  600000), Lithium bis(trifluoromethanesulfonyl)imide ( $\text{LiC}_2\text{F}_6\text{NO}_4\text{S}_2$ , 99.95% trace metals basis) and Acetonitrile (ACN, anhydrous, 99.8%) were purchased from Sigma Aldrich. Materials were introduced in an Ar-filled glovebox at  $\text{O}_2 < 1\text{ppm}$  and  $\text{H}_2\text{O} < 1\text{ppm}$ .

2.67g of PEO was dissolved in 77g ACN. 1.67g of LiTFSI was added and stirred with a spatula. 12g of LLZO powder was added and stirred again with a spatula. These mass ratios were chosen to result in approximately even volumetric parts of ceramic and polymer within the dried films. The EO:Li molar ratio is 10.4 : 1. The total solid content of the slurry is 17.5wt% ( $m_{\text{PEO}} + m_{\text{LiTFSI}} + m_{\text{LLZO}}/m_{\text{total}}$ ).

The container was sealed under Argon with Parafilm® and then mixed in a planetary centrifugal mixer (Thinky ARE-250). Conditions were as follows: Mixing at 2000rpm for 2min and degassing at 2000rpm for 2min30s. The process was repeated 7 times to yield approximately 700ml of slurry. The containers were kept separate and sealed until curtain deposition.

### Rheology

Viscosity measurements were performed using a commercial rheometer (MCR 302; Anton Paar) in concentric cylinder geometry using a double gap cylinder (DG26.7; sample volume 4 ml). Temperature was held at 25 °C and a frequency sweep was performed between 1 s<sup>-1</sup> and 1000 s<sup>-1</sup>.

### Structural characterization

X-ray diffraction was carried out with a Rigaku Smartlab. Samples were measured at 45kV, 200mA with Cu k-alpha radiation in parallel beam mode. 5° Soller slits and an incident slit of 0.5mm was used. Rigaku's Hypix-3000 detector was used in 1D mode to acquire symmetric  $\theta/2\theta$  scans from 13° to 60°.

### SEM imaging

Cross-sections of the coated solid electrolytes are prepared with a Hitachi IM4000 Ion Milling System, which uses a broad, low energy Argon ion beam to polish wide, cross-sectional cuts. SEM images were acquired by a Hitachi SU8200. A coupled secondary electron/backscattered electron (SE/BSE) mode with 60% SE suppression was selected for image acquisition. Acceleration voltage was 2kV; emission current was 10.5 $\mu\text{A}$ .

### Impedance Measurements

Electrochemical impedance measurements are performed with a Bio-Logic VSP-300 potentiostat. The excitation voltage was set to 20mV, and the frequency was scanned from 100mHz to 500kHz. The data was fitted with Z Fit, a part of the EC-Lab® software. An equivalent circuit consisting of a bulk resistance  $R_{\text{bulk}}$  in parallel with a constant phase element  $CPE_{\text{bulk}}$  is selected. Blocking electrodes are represented by an additional  $CPE_{\text{blocking}}$  in series. The ionic conductivity was calculated according to  $\sigma = d/(A \times R_{\text{bulk}})$ , where  $d$  is the measured thickness of the solid electrolyte and  $A$  is the area of the electrodes (2.01 cm<sup>2</sup>).

### Coating Setup

The coating setup is a custom design using aluminum profiles as a frame (**Fig. S2**). The conveyor belt system is constructed with an electric drive (motor and speed control) by Oriental Motors connected to rollers. The maximum coating speed is 3.5m/s, limited by the chosen gear ratio. Volume flow can be regulated linearly up to 2210ml/min (Ismatec VC280). An open reservoir is placed on top of the coating die to minimize volume flow ripples. For steady state operation the minimum slurry volume within the system is approximately 500ml. During coating the slurry is agitated with a magnetic stirrer in the reservoir (**Fig. S3**). The curtain height can be adjusted up to 20cm. 4 microscope slides (25mm x 75mm) are placed on a carrier and coated at a time when passing through the curtain. The slides provide a rigid substrate to prevent warping during drying.

### Operational Parameters

The deposition is a metered process. Therefore, the wet thickness  $h_{wet}$  of the deposited film can be calculated as follows:

$$h_{wet} = \dot{V} / (u_{web} \times b),$$

where the volume flow  $\dot{V}$  was measured and the curtain width  $b$  is given by the coating head. The web speed  $u_{web}$  is calculated using the motor speed  $\omega_{motor}$ , the gear ratio  $r_{gear}$ , and the diameter of the drive roll  $d_{roll}$ :

$$u_{web} = \omega_{motor} \times r_{gear} \times \pi \times d_{roll}.$$

To estimate the dry thickness  $h_{dry}$ , the wet thickness is multiplied by the volumetric solid content  $sc_{vol}$ , which is calculated to be  $5.75\% = 100\% \times (V_{PEO} + V_{LiTFSI} + V_{LLZO}) / V_{total}$ ,

$$h_{dry} = h_{wet} \times sc_{vol}.$$

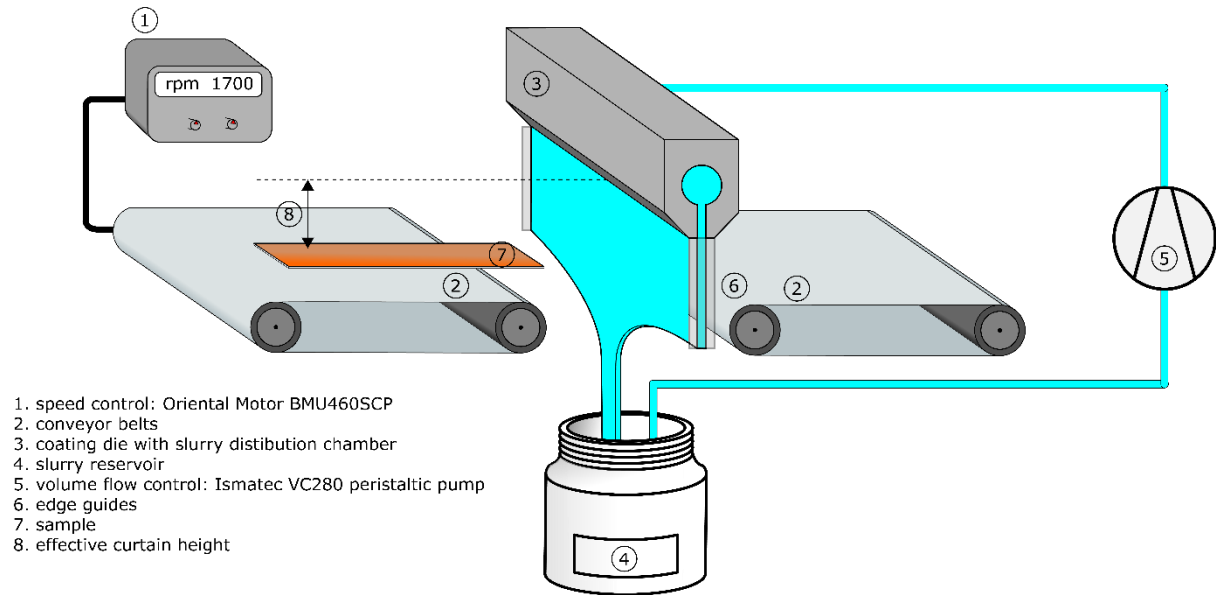
The values in **Table S2** were used to estimate the dry thicknesses for the two coating conditions to be 15.2 $\mu$ m and 30.5 $\mu$ m respectively.

### Sample Preparation

Glass slides were covered with Cu-foil. The substrates were cleaned with an acetone wipe and subsequent air plasma treatment for 1min (Harrick Plasma, PDC-32G). The volume flow was set to 1327ml/min and the curtain height was kept constant at 4.5cm, which resulted in a stable curtain. Web speeds of 41.7m/min and 83.4m/min were selected to achieve different film thicknesses. After deposition the samples are placed in an oven to dry at 60°C under vacuum for 3h. The samples were then transferred to an Ar filled glovebox. In the antechamber they are left under vacuum for an additional 24h to remove residual moisture. Electrodes with a diameter of 18mm were punched out. A second Cu foil disk was added on top for a blocking electrode setup. A PE separator ring (outer diameter 20mm / inner diameter 16mm) was sandwiched in between to avoid short circuiting at the edges from misalignment. Under ambient conditions the samples were calendered with a pellet press at 2 tons for 1min between two aluminum blocks preheated to 100°C. The electrode stack underwent another drying procedure (overnight under vacuum) and was transferred back to an Ar glovebox. There custom designed cells were assembled (**Fig. S3**).

## Supplemental Data Items

**Figure S1. Coating Setup, Related to Figure 3A**



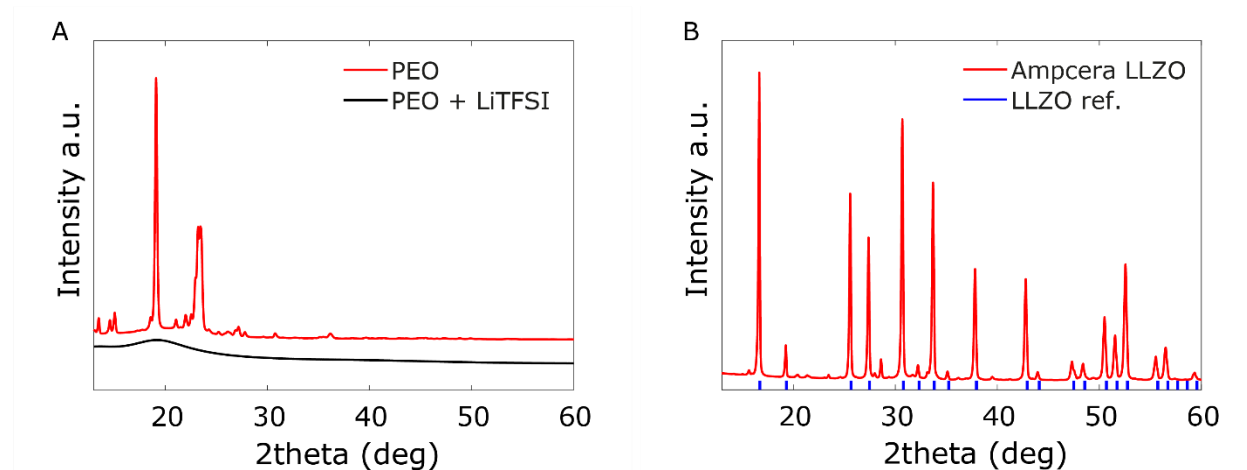
Schematic of the coating setup with relevant components indicated.

**Figure S2. Slurry Reservoir, Related to Figure 3A**



Slurry reservoir for continuous curtain operation. During deposition the slurry is agitated by a magnetic stirrer.

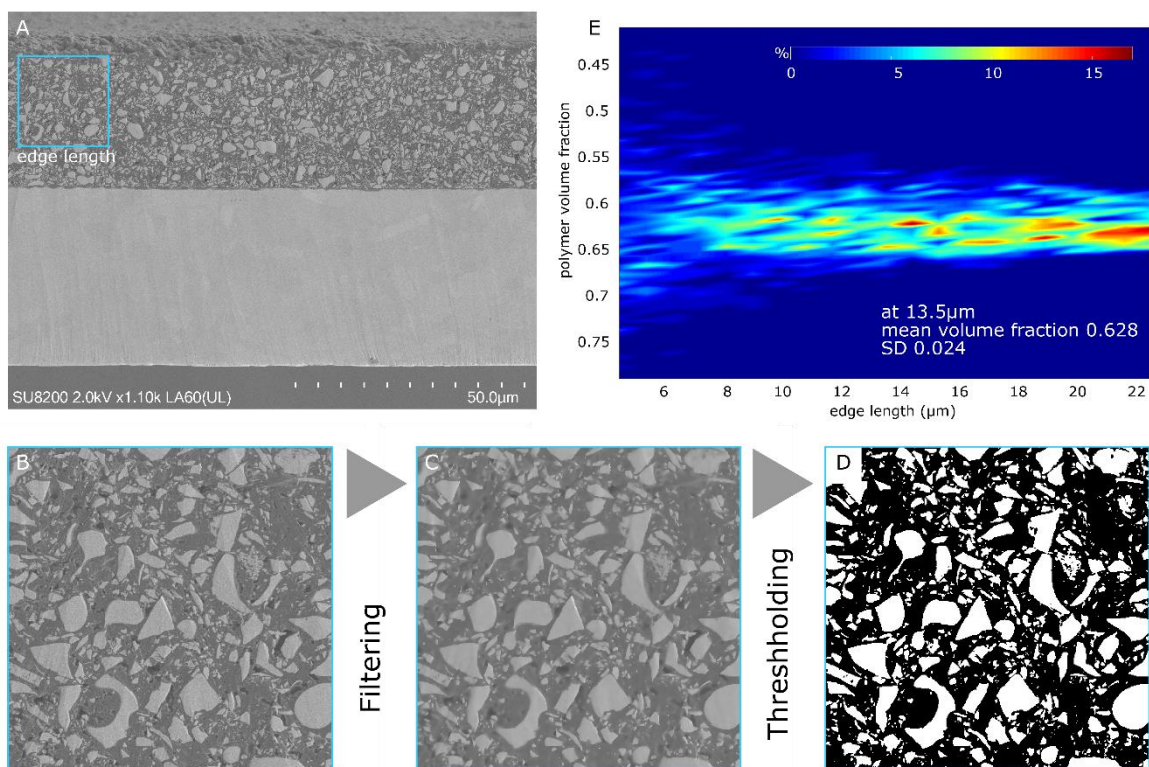
**Figure S3. Structural Characterization, Related to Figure 3F**



A) X-ray diffraction measurements on crystalline PEO powder (red) and PEO electrolyte films with LiTFSI salt (black). The broad peak suggests a mainly amorphous structure when LiTFSI is incorporated in the polymer at a 10.4:1 molar ratio of EO:Li. B) The LLZO powder shows the cubic LLZO phase.

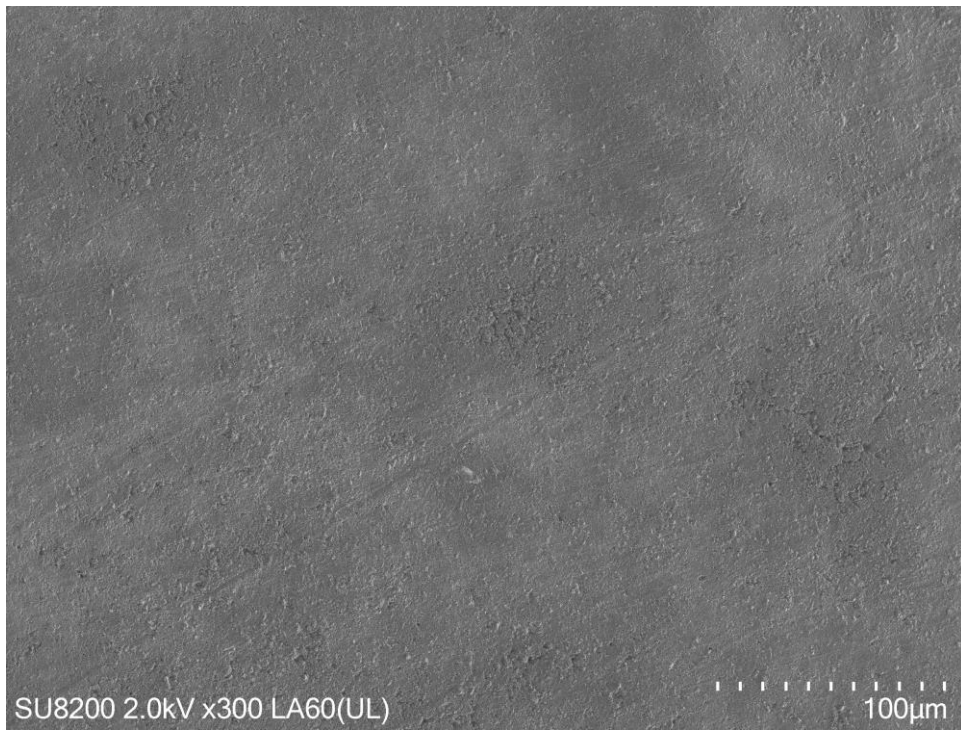


**Figure S4. Scale Space Analysis, Related to Figure 4A, B**



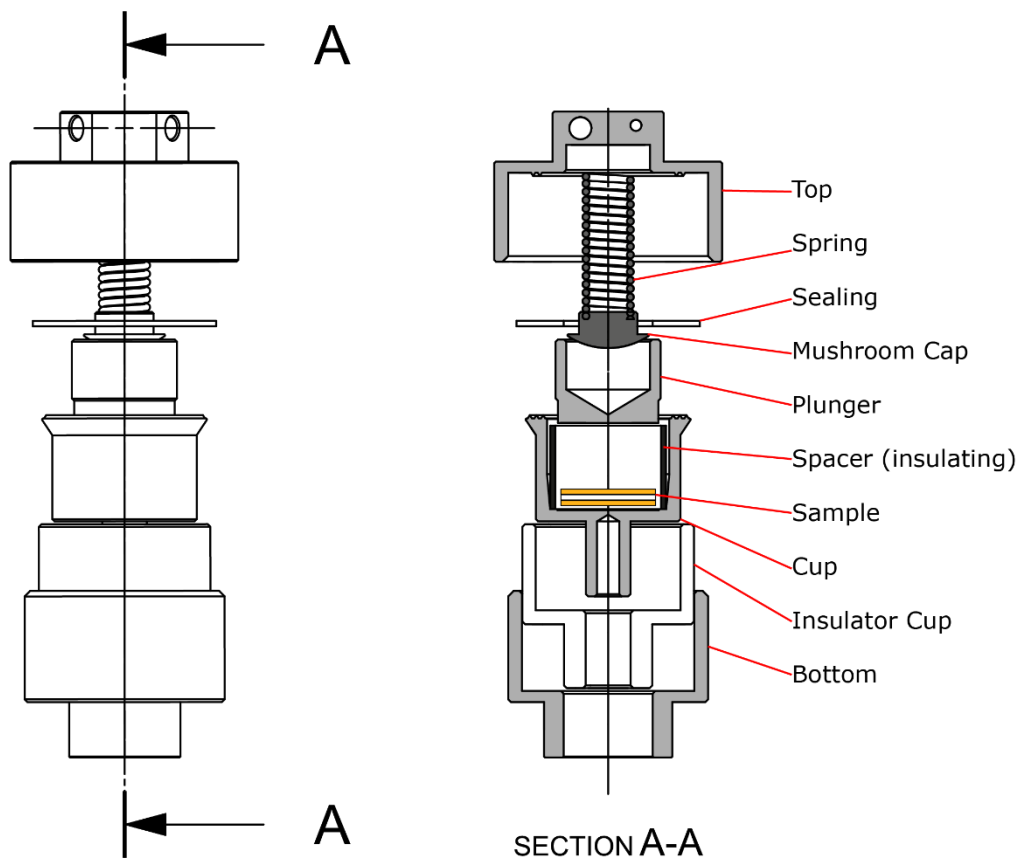
Scale space analysis is performed on the electrolyte films to quantify the uniformity. From a SEM image (A), a subsection of a specific edge length is selected (B). The selected part is smoothed with an anisotropic diffusion filter (C) and subsequently thresholded (D), with the polymer matrix in black and ceramic particles in white. The volume fraction of the polymer phase is calculated for 100 samples and depends on the subsection edge-length (E). At an edge length of around  $13.5\mu\text{m}$ , the calculated polymer volume fraction stabilizes at around 0.628 with a standard deviation of 0.024. This suggests that for the materials used in this study, films should be at least  $13.5\mu\text{m}$  in thickness to exhibit uniform lithium ion conduction in the through plane direction.

**Figure S5. SEM Top View, Related to Figure 4A, B**



Top view of electrolyte films.

**Figure S6. Cell Design, Related to Figure 4C, D**



Schematic of custom-made cells for electrochemical impedance spectroscopy measurements.

**Table S1. Operational Parameters, Related to Operational Parameters**

density LiTFSI (g/cm <sup>3</sup> )	1.33
density LLZO (g/cm <sup>3</sup> )	5.13
density PEO (g/cm <sup>3</sup> )	1.12
density ACN (g/cm <sup>3</sup> )	0.786
gear ratio $r_{gear}$	4/10
flow rate $\dot{V}$ (ml/min)	1327
motor speed $\omega_{motor}$ (rpm)	800/1600
drive roll diameter $d_{roll}$ (mm)	41.5
web speed $u_{web}$ (m/min)	41.7/83.4
curtain width $b$ (mm)	60

Material properties and operational parameters for the coating runs.

**Table S2. Parameters of Equivalent Circuit Model, Related to Figure 4C, D**

Thickness	Temp [°C]	CPE <sub>blocking</sub>	a <sub>blocking</sub>	CPE <sub>bulk</sub>	a <sub>bulk</sub>	R <sub>bulk</sub> [Ω]
27.8 μm	20	0.000003031	0.8766	1.871E-08	0.8203	403.4
	30	0.000003526	0.8751	1.64E-08	0.8391	142.2
	40	0.000004531	0.8645	5.887E-09	0.9059	54.29
	50	0.000005778	0.8517	6.257E-09	0.9	27.27
	60	0.000008126	0.8223	1.776E-09	0.9	15.26
	70	0.00001208	0.797	1.438E-22	0.9	9.203
13.8 μm	20	0.000002681	0.8909	4.427E-08	0.8021	259.1
	30	0.000002445	0.912	4.655E-08	0.8054	88.44
	40	0.000002846	0.9064	2.336E-08	0.8598	32.65
	50	0.000003428	0.8964	7.44E-09	0.9288	16.32
	60	0.000004387	0.881	3.685E-09	0.9	9.023
	70	0.000008926	0.8264	1.515E-22	0.9	4.76

Results from fitting the equivalent circuit model to impedance measurements. The model is depicted in the inset of **Fig. 4D**.